LA-UR-21-20790 (Accepted Manuscript)

Compositional screening of Ce-doped (Gd,Lu,Y)3(Al,Ga)5O12 ceramics prepared by quenching from melt and their luminescence properties

Barta, Jan
Pestovich, Kimberly Shay
Valdez, James Anthony
Wiggins, Brenden W.
Richards, Cameron Gregory
Smith, Erick
Clayton, Jessica H.
Smalley, Duane
Mcclellan, Kenneth James

To be published in: Journal of Alloys and Compounds

DOI to publisher's version: 10.1016/j.jallcom.2021.161687

Permalink to record: http://permalink.lanl.gov/object/view?what=info:lanl-repo/lareport/LA-UR-21-20790

Compositional screening of Ce-doped $(Gd,Lu,Y)_3(Al,Ga)_5O_{12}$ ceramics prepared by quenching from melt and their luminescence properties

J. Bárta, K.S. Pestovich, J.A. Valdez, B.W. Wiggins, C. Richards, E. Smith, J.H. Clayton, D. Smalley, K.J. McClellan

PII: S0925-8388(21)03096-6

DOI: https://doi.org/10.1016/j.jallcom.2021.161687

Reference: JALCOM161687

To appear in: *Journal of Alloys and Compounds*

Received date: 28 June 2021
Revised date: 12 August 2021
Accepted date: 21 August 2021

Please cite this article as: J. Bárta, K.S. Pestovich, J.A. Valdez, B.W. Wiggins, C. Richards, E. Smith, J.H. Clayton, D. Smalley and K.J. McClellan, Compositional screening of Ce-doped $(Gd,Lu,Y)_3(Al,Ga)_5O_{12}$ ceramics prepared by quenching from melt and their luminescence properties, *Journal of Alloys and Compounds,* (2021) doi:https://doi.org/10.1016/j.jallcom.2021.161687

Compositional screening of Ce-doped $(Gd,Lu,Y)_3(Al,Ga)_5O_{12}$ ceramics prepared by quenching from melt and their luminescence properties

Bárta, J.[a,b,*], Pestovich, K. S.[a], Valdez, J. A.[a], Wiggins, B. W.[a], Richards, C.[a], Smith, E.[c], Clayton, J. H.[d], Smalley, D.[d], McClellan, K. J.[a]

[a]Materials Science and Technology division, Los Alamos National Laboratory, Los Alamos, NM 87545, USA

[b]Faculty of Nuclear and Physical Engineering, Czech Technical University in Prague, Břehová 7, 115 19 Prague 1, Czech Republic

[c]Physics division, Los Alamos National Laboratory, Los Alamos, NM 87545, USA

[d]Mission Support and Test Services LLC, Nevada National Security Site, 2900 East Road, Los Alamos, NM 87544, USA

[*]**Corresponding author**: jan.barta@fjfi.cvut.cz

Abstract

Quenching from the melt using an Optical Floating Zone furnace was investigated as a possible high-throughput preparation method in order to screen novel scintillating materials. To validate this method, polycrystalline rare-earth aluminium garnets and yttrium gallium aluminium garnets were synthesized and characterized by X-ray diffraction, photoluminescence and radioluminescence emission spectra as well as radioluminescence imaging and compared to the previously reported properties of those materials. In order to achieve rapid, but quantitative comparison of the materials, pellets fabricated from the synthesized powders were sintered; two different sintering conditions were investigated and compared. A simplistic energy deposition and light absorption model for brightness of opaque samples under X-ray irradiation was developed to estimate the relative scintillation efficiency of the materials. Based on the results, $Y_3Al_5O_{12}$, $LuY_2Al_5O_{12}$ and $GdY_2Al_5O_{12}$ seem to have the highest scintillation efficiency among the prepared samples.

Keywords: phosphors; rapid solidification, quenching; sintering; luminescence; X-ray diffraction

1. Introduction

Inorganic scintillators, materials that are used to down-convert ionizing radiation into visible, UV or IR spectral range, are nowadays broadly utilized in medical imaging, high-energy physics, homeland security, electron microscopy and many other applications (see [1] and references therein). These varied applications for scintillating materials impose rather diverse and often contradictory requirements on the various properties of those materials, such as emission wavelength, light yield, decay time, afterglow, temperature stability, density or the level of inherent radioactivity [1]. For new applications, users are usually limited to off-the-shelf scintillators that may not fulfil all the requirements needed, because the development of a new scintillator that satisfies these requirements is a laborious, costly and time-consuming task. For that reason, the research team in the Materials Science and Technology division of the Los Alamos National Laboratory started developing physics-based predictive models and performance models involving machine-learning [2,3] that should allow to select a new scintillating material that would satisfy the requirements using multi-parametric optimization. In order to train such performance models, it is necessary to provide them with reliable input data for various properties of compounds within as large chemical space as possible. Therefore, this modelling effort needs to be coupled with rapid screening and characterization that will supply reasonably accurate values for a broad range of properties. Some properties are strongly affected by the preparation technique used; therefore, a single universal preparation technique would be beneficial for obtaining the most internally consistent input data. Ideally, the synthesized materials should have properties similar to the optimal material form (often single crystals) as well. This study is focused on the development and validation of a high-throughput synthesis method (quenching from the melt) on a rather well-explored group of materials – rare-earth garnets – by a comparison of the obtained values with literature.

Rare-earth containing garnets are crystalline materials with a rather intricate cubic structure (space group $Ia\overline{3}d$, no. 230), having a general formula $\{A\}_3[B]_2(C)_3O_{12}$ that contains three types of coordination polyhedra. The dodecahedral position {A} with a D_2 (222) symmetry is surrounded by 8 oxygen atoms in a distorted tetragonal anti-prism and accommodates very large ions, whereas both the octahedral [B] site and tetrahedral (C) site are much smaller [4,5]. In the most explored so-called rare-earth “aluminate” and "gallate" garnets, rare-earth metal ions mostly occupy the dodecahedral site – $\{RE\}^{3+}$, whereas smaller Al^{3+} and Ga^{3+} ions are distributed among both B and C sites, resulting in a general formula $\{RE\}_3(Al,Ga)_5O_{12}$. Although their crystal radii would suggest that in mixed Al+Ga garnets the smaller Al^{3+} ions are preferably situated in the smallest tetrahedral sites and Ga^{3+} in the larger octahedral ones, structural refinements and/or NMR analyses of single crystals often reveal an opposite trend [6]. Additionally, very high temperatures required for single crystal growth of garnets cause a non-negligible fraction of $\{RE\}^{3+}$ to be present in the octahedral position as well, causing so-called anti-site defects (such as Lu_{Al}, Y_{Al}), shallow electron traps that severely limit the performance of Ce-doped aluminate garnets [7].

$\{RE\}_3Al_5O_{12}$ are thermodynamically stable and congruently melting compounds when the size of the rare-earth ion is rather small; their stability decreases with increasing crystal diameter of rare earth ions so that only Tb–Lu form stable aluminate garnets [5]. Thus, gadolinium aluminium garnet is an incongruently melting compound that can be prepared by low-temperature techniques [8], whereas rare-earth ions larger than Eu do not form aluminate garnets at all. The incorporation of larger Ga broadens the region of garnet phase stability to (Nd–Lu, Y) in $\{RE\}_3Ga_5O_{12}$. Within this range, garnet materials are often found to form substitutional solid solutions, creating a continuous range of similar compounds that influence their properties [9].

In order to achieve high-throughput screening of materials, a relatively fast preparation technique able to reliably produce material with properties comparable to desired material form (e.g. single crystals) is required. In this work, a modification of optical floating zone (OFZ) method was used to rapidly synthesize polycrystalline materials by melting. OFZ growth is a crucible-less single crystal preparation technique utilizing a powerful light source (laser, incandescent light or arc discharge) focused onto a very small spot, leading to melting of the initial solid material. By moving the solid material through the hot zone, single crystalline materials can be grown on a support (seed) rod [10]. A rather unique application of this method is quenching of the melt, which has similar effects to the procedure used in [11] to study solidification of $Y_3Al_5O_{12}$ from the melt. In the OFZ modified for melt-quenching, the formed melt is allowed to drop into a cooled ceramic receptacle or even liquid to rapidly solidify and form polycrystalline material. Thus, the segregation coefficient effects, an important issue during the growth of single crystals from the melt [12], should be somewhat mitigated as there is no continuous long-lasting contact between the formed crystal and the melt. The other main advantages of this method for screening are: a rather large amount of material prepared within a short time, the ability to change the atmosphere at will and the possibility to easily obtain even solid materials with extremely high melting temperatures. Compared to the much more common solid state reactions, quenching from the melt offers much higher sample throughput, as solid state reactions require several days of heat treatment at very high temperatures to obtain phase-pure samples, while quenching from the melt is finished within a few hours and allows the synthesis of materials that are very hard to prepare as a phase-pure sample by solid state reactions (e.g. $YAlO_3$).

In this work, quenching from the melt was evaluated as a rapid preparative method for a very quick and reproducible synthesis of Ce-doped garnet materials within the $Lu_3Al_5O_{12}$ – $Y_3Al_5O_{12}$ – $Gd_3Al_5O_{12}$ chemical region and between $Y_3Al_5O_{12}$ and $Y_3Ga_5O_{12}$. Its potential for screening was assessed by observing the changes in their structural and luminescence properties, including photoluminescence spectra, decays and radioluminescence spectra, and comparing the observations to the known properties of such materials prepared by classical preparation methods. Additionally, the possibility of direct comparison between such materials was explored using sintering conditions determined for each particular sample in order to achieve a comparable morphology of sintered pellets with well-defined geometry. Radioluminescence imaging of such pellets under continuous X-ray irradiation was investigated as a reliable and fast technique to achieve an internally consistent dataset of scintillating properties and to estimate their relative light yield, required for further screening studies.

2. Experimental

2.1. *Sample preparation*

Polycrystalline garnet samples studied in this work were prepared by quenching from the melt using single-lamp, single-mirror optical floating zone furnace FZ-S15065X(HV) (Asgal Corp., Japan) equipped with a 6.5 Xe arc lamp. First, stoichiometric amounts of metal oxides (99.997% Gd_2O_3; 99.997% Lu_2O_3; 99.9998% Y_2O_3; 99.99% Ga_2O_3; 99.99% Al_2O_3 and 99.997% CeO_2) according to the desired sample composition (see Tab. 1) were weighed out, mixed for 30 min in plastic jars with a plastic ball using SPEX 8000 mill and isostatically pressed into compact rods. For all samples, 1 molar % Ce as a dopant was used relative to all rare-earth metal ions, leading to a general formula $\{RE\}_{2.97}Ce_{0.03}(Al,Ga)_5O_{12}$. The rods were heated in the OFZ furnace under flowing air (in order to prevent formation of oxygen vacancies) until the material melted and were then moved through the hot zone so that the melt dropped into a cooled Al_2O_3 crucible serving as a receptacle. The melting process for a typical 10-gram batch usually took less than an hour. Polycrystalline solid material resulting from quickly solidified melt was then ball-milled in SPEX 8000 mill in corundum milling jars with corundum ball for 60 minutes and sieved ($\leq$ 45 μm) to yield fine powders.

2.2. Pellet fabrication and characterization

In order to quantitatively compare the luminescence properties of samples, the sieved powders were mixed with 0.5 wt. % ethylene bis(stearamide) (EBS) binder for 30 min in plastic jars with a plastic ball using the SPEX 8000 mill and pressed into pellets 13 mm in diameter at uni-axial pressure of 100 MPa. The first batch of pellets was sintered at 1700 °C / 4 h in air on alumina tray, yielding dense and durable pellets (*"stage 3"* [13] sintered pellets). Both sides of pellets were then ground to parallel flat surfaces using Struers Accutom-50 and a diamond cup wheel to remove potential surface contamination. The resulting pellets were then annealed at 1200 °C for 12 hours in air to remove any residual organic impurities.

Due to inhomogeneous coloration and light output across the surface of these pellets, a low-temperature sintering of the initial powder was also applied to obtain consistent results. This second batch of pellets was sintered for 4 hours in air at a sintering temperature sufficient to induce necking (*"stage 2"* sintering, see below), using 10 °C / min as both the cooling and the heating rate. For the determination of required *"stage 2"* sintering temperature, Netzch DIL 402 c dilatometer was utilized: pellets with diameter of 5.33 mm (4.6 to 6.8 mm long) pressed at 200 MPa were heated at 2.5 °C / min up to 1550 °C and changes in their length L during heating were recorded. The required *"stage 2"* sintering temperature was determined as the peak in dL/L_0, where the initial increase in L

due to the thermal expansion started to be overcome by shrinkage due to sintering. The temperatures of such peaks are summarized in Tab. 1.

X-ray powder diffraction patterns of samples were recorded on a Bruker Nano D8 Advance diffractometer equipped with a LynxEye XE-T position sensitive detector (range of 2.9° 2θ) and copper X-ray tube (Cu-$K_{\alpha1,2}$, $\lambda = 1.54186$ Å; 40 kV, 40 mA). The X-ray beam was conditioned with a Bruker Trio optic using the Göbel mirror setting and the 2.5° incident and receiving Soller slits. Diffraction patterns were fitted and the lines identified and indexed based on the ICSD database by the Rigaku SmartLab II suite. The lattice parameters of garnet phase *a* along with sample displacement correction were determined using weighted linear regression from observed peak positions. Optical absorption spectra of pellets were recorded on a Varian Cary 5000 spectrophotometer.

2.3. *Luminescence characterization*

Room-temperature photoluminescence properties of the pellets were measured on a PTI Quantamaster spectrofluorometer equipped with a 75 W Xe arc lamp as a light source, diffraction grating monochromators for both excitation and emission pathways, and Hamamatsu R928P photomultiplier tube as detector. The measured emission spectra (PL) were spectrally corrected using a built-in spectral correction curve. Because of a relatively large contribution of scattered light in the spectra of samples excited at 468 nm, the spectral shape in the high-energy side of the Ce^{3+} 5*d* – 4*f* emission band was approximated by the high-energy side of the PL spectra excited at 350 nm to ensure a good fit of the emission band. The photoluminescence decay curves were measured by a Horiba DeltaPro apparatus using a 421 nm Horiba nanoLED as the excitation source. In order to isolate the excitation light from the luminescence, the decay curves were recorded with a 460 nm cut-off filter.

Room-temperature radioluminescence emission spectra (RL) were measured on a custom-built setup equipped with Mo X-ray tube (17.3 keV; 50 kV, 40 mA); the emitted light was collected by an optical cable into a SpectraPro 2300i spectrometer (Princeton Instruments) equipped with a CCD camera (Pixis 2KB EUV). The measured emission spectra were corrected for quantum efficiency of the camera and estimated efficiency of the diffraction grating used.

Spatially resolved radioluminescence images of pellets were recorded at the SEALab facility (Scintillator Evaluation and Assessment Laboratory) of the Nevada National Security Site (NNSS), Los Alamos in front-face-imaging configuration – see Fig. 1. The apparatus consists of a Comet XRS-225VF CW X-ray tube (225 kV, W anode) serving as the excitation source, thin reflecting pellicle in order to reflect the light from the scintillators, sample holder and Andor Neo 5.5 sCMOS camera. In the front-face-imaging arrangement, the collimated X-rays pass through the pellicle onto the sample surface, where they induce scintillation; the emitted light is then reflected by the pellicle into the camera to be recorded (spectrally unresolved photon counting). The end-point energy was chosen as 225 keV and the X-ray spectrum features two main prominent characteristic X-ray lines (W-$K_{\alpha,\beta}$) at 59 and 67 keV; a spectrum simulated in GEANT4 (see Supplementary Information Fig. SI_5) was used for further calculations. X-ray dose distribution across the sample holder with up to 5 measured pellets was observed using 6 small Lu_2SiO_5:Ce crystals placed within the holder as standards and by a separate measurement of DRZ® High scintillator screen (Gd_2O_2S:Tb). Relative scintillation intensity of pellets was evaluated as brightness at maximum of the Gaussian fit of the brightness histogram for the given sample. These values were then corrected for spectral response of the camera and beam profile non-uniformity.

3. Results and discussion

3.1. Structural properties

X-ray powder diffraction analysis of the *“stage 3”* sintered pellets revealed that the samples contained a cubic phase consistent with the $Ia\overline{3}d$ garnet structure (see Fig. 2) in all but one sample. In the case of $Gd_3Al_5O_{12}$, the sample consisted only of orthorhombic perovskite phase ($GdAlO_3$, space group Pnma) and a minute amount of corundum (α-Al_2O_3). This behavior is consistent with the well-known lower stability of this garnet phase compared to the perovskite [5]; $Gd_3Al_5O_{12}$ melts incongruently and can be prepared e.g. by low-temperature chemical methods, but usually with perovskite impurity [8]. In several samples, a small corundum impurity (rhombohedral α-Al_2O_3, space group $R\overline{3}c$) was also found, close to its limit of detection (almost indistinctive peaks at 25.8° and 43.4° 2θ). Corundum probably formed during melting either due to a small non-stoichiometry of the initial mixture, or because of the easy occurrence of anti-site defects in the garnet lattice and thus, slightly RE-rich garnet phase, i.e. $\{RE\}_3Al_{2(1-x)}\{RE\}_{2x}Al_3O_{12}$ [14,15]. Another possibility is the abrasion of the milling media (corundum jar, ball) used for pulverizing the samples. The presence of corundum, however, does not significantly influence the evaluation of Ce^{3+} luminescence from the garnet samples. Another minor impurity with a diffraction peak at 22.0° 2θ was observed in $Gd_2YAl_5O_{12}$, $Lu_2YAl_5O_{12}$ (see Fig. 2) and $Y_3AlGa_4O_{12}$, but due to the lack of other visible lines, it could not be unambiguously ascribed to a phase that could be expected in the samples.

Tab. 1 – Composition, lattice parameters, dilatometer peak temperature, sintering temperature used and achieved density (% of theoretical density TD) of sintered garnet pellets; all samples were doped with 1 mol. % Ce

Chemical formula	Lattice parameter *a* [Å][1]	DIL peak temperature [°C]	Sintering temperature used [°C]	% TD (13 mm pellet)	
	stage 3		*stage 2*	*stage 2*	*stage 3*
$GdY_2Al_5O_{12}$	12.043(1)	1172	1175	67 %	76 %
$Gd_2YAl_5O_{12}$	12.082(1)	1148	1150	64 %	77 %
$Gd_3Al_5O_{12}$	*perovskite*	-[1]	-[1]	-[1]	-[1]
$Gd_2LuAl_5O_{12}$	12.051(2)	1199	1200	66 %	75 %
$GdLu_2Al_5O_{12}$	11.979(3)	1157	1150	66 %	73 %
$Lu_3Al_5O_{12}$	11.916(3)	1204	1200	68 %	75 %
$Lu_2YAl_5O_{12}$	11.947(1)	1184	1175	67 %	74 %
$LuY_2Al_5O_{12}$	11.979(2)	1145	1150	69 %	73 %
$Y_3Al_5O_{12}$	12.012(2)	1168	1175	68 %	78 %
$Y_3Al_4GaO_{12}$	12.060(2)	1143	1150	65 %	77 %
$Y_3Al_3Ga_2O_{12}$	12.107(4)	1047	1050	66 %	92 %
$Y_3Al_2Ga_3O_{12}$	12.167(2)	977	975	65 %	85 %
$Y_3AlGa_4O_{12}$	12.202(3)	not meas.	975	69 %	79 %
$Y_3Ga_5O_{12}$	12.263(10)	-[2]	-[2]	-[2]	-[2]
$GdLuYAl_5O_{12}$	12.011(1)	1213	1200	67 %	74 %

[1] not a garnet phase, excluded from further analysis,

[2] Ce^{3+} luminescence totally quenched, excluded from further analysis

The lattice parameters *a* determined from the diffraction patterns for each garnet composition studied in this work (see Tab. 1) were arranged and plotted as a consecutive series of solid solutions on Fig. 3, with $GdLuYAl_5O_{12}$ positioned last. The experimental values lie on reasonably straight lines between each end-point garnet phase in accordance with the Vegard's rule [16]. Similarly, the lattice parameter of $GdLuYAl_5O_{12}$ perfectly matches the average *a* between $GdLu_2Al_5O_{12}$ and $GdY_2Al_5O_{12}$ (shown as a dashed line in Fig. 3). This strongly suggests that all garnet samples examined in this work formed random substitutional solid solutions; thus, the unit cell volume of studied garnet varies due to the average spatial requirements of ions present in the lattice.

The lattice parameters of end-point garnet phases reported in literature match the lattice parameters of the samples and trends, confirming their correct composition. However, the experimental values are (with some exceptions, see Ga discussion below) always slightly higher than the corresponding reference value. Considering that the powders were prepared by melting and subsequent high-temperature sintering, the increase might partially result from the presence of anti-site defects such as Lu_{Al} (Lu^{3+} on the octahedral site instead of Al^{3+}) [15]. However, the main part of this increase can be successfully explained by 1% doping of the large Ce^{3+} ions (Shannon's crystal radius of Ce^{3+} in coordination number 8 is 1.283 Å; [17]) substituting for the smaller rare-earth ions (Lu^{3+}: 1.117 Å; Y^{3+}: 1.159 Å; Gd^{3+}: 1.193 Å).

In $Y_3(Al,Ga)_5O_{12}$ garnets examined in this work, however, the lattice parameters are consistently lower than the corresponding literature values or trends. This is probably caused by the volatility of Ga, a common issue during growth of Ga-containing single-crystalline garnets in inert atmosphere, as the Ga^{3+} in the melt tends to be reduced to lower-valence volatile oxides [18]. To counter this behavior, a small amount of oxygen is usually added to the inert atmosphere so as not to oxidize iridium crucibles excessively while limiting Ga losses. Although all studied materials were prepared and sintered in air, some loss of Ga during these operations cannot be excluded due to very high temperatures used.

The investigation into the post-synthesis processing (both sintering options) aimed to determine, which of the possible approaches – long sintering at very high and arbitrary temperatures ("stage 3") and short sintering at a moderate temperature determined in a separate measurement ("stage 2") – is more suitable for self-consistent evaluation of the samples. In particular, the microstructure of the samples, strongly influenced by their theoretical density (% TD, see Tab. 1), represents a very important contribution to absolute luminescence intensity microstructure of samples due to change in light scattering within the samples. The *"stage 3"* sintered pellets studied in this work had a rather large spread of densities with respect to their theoretical values, i.e. 73 – 92 % TD. However, all the *"stage 2"* sintered pellets had comparable theoretical densities, with most pellets being within 67 – 68 % TD (see Tab. 1). This indicates that the use of the peak temperature from dilatometer measurements is a reasonably valid procedure for sintering of pellets to a comparable degree. That allows quantitative comparison of their luminescence emission intensity, provided that a similar % TD relates to comparable microstructure and gives a comparable degree of light scattering.

3.2. Photoluminescence properties

The photoluminescence spectra of the studied samples feature an intense broad band peaking between 500 and 580 nm (see Fig. 4 and Supplementary Information Fig. SI_1), corresponding to the emission doublet between the lowest-lying 5*d* excited level of Ce^{3+} ($5d_1$) and its two 4*f* states ($^2F_{5/2}$ and $^2F_{7/2}$) in a given host. Actually, both latter states are just an approximation for the Ce^{3+} ^2F level that is split into seven Stark sub-states because of the low Ce^{3+} site symmetry in garnets (D_2, 222) [19]. The two main groups of these Stark sub-states (~ $^2F_{5/2}$ and $^2F_{7/2}$) are separated by ca. 2000 $cm^{-1} \equiv 0.248$ eV in most luminescent materials [19]. The excitation spectra feature two broad excitation bands at ~ 450 and ~ 350 nm corresponding to the transition from the $^2F_{5/2}$ state of Ce^{3+} into the first and second excited 5*d* levels, respectively.

In some samples, small emission lines were observed at ~ 685 and ~693 nm under excitation at 468 nm, corresponding to the R-line doublet of a relatively common Cr^{3+} impurity emitting from garnet lattice or Al_2O_3, respectively [20].

The changes in emission band positions reflect the influence of the surrounding crystal field on the Ce^{3+} 5*d* levels and their splitting. The observed emission band positions and their shifts are fully in accordance with literature about Ce-doped garnets [9,21,22], with Gd causing red shift of the emission band and Lu causing its blue shift in comparison to Y (see Supplementary Information Fig. SI_1). Substitution of Al by Ga results in a strong blue shift of the Ce^{3+} 5*d* – 4*f* emission doublet (see Fig. 4). For a detailed description of underlying physics, the reader is referred to a comprehensive review paper by [23].

The positions of both Ce^{3+} emission bands were obtained by fitting the room-temperature photoluminescence emission spectra transformed into relative power emitted per unit energy (~ W/eV). Both components of the room-temperature emission band doublet represented as the peak energy show a reasonably linear behavior between most end-point garnets (see Fig. 5 and Supplementary Information Tab. SI_1). Only the $Gd_2(Lu/Y)Al_5O_{12}$ samples slightly deviate from linear behavior and are somewhat blue-shifted compared to the expected value. The average separation of the PL emission components is ~ 1500 cm^{-1}, a slightly lower value than the commonly used value of 2000 cm^{-1} between $^2F_{5/2}$ and $^2F_{7/2}$ states.

Photoluminescence decay curves for the Ce^{3+} 5*d* – 4*f* transition excited through 421 nm pulsed nanoLED were for most samples reasonably single exponential, with decay times within 49 – 58 ns (see Fig. 5 and Supplementary Information Tab. SI_1). Such values are fully consistent with the parity-allowed Ce^{3+} emission from garnets. Photoluminescence decay times follow compositional trends similar to emission energy evolution, with higher energy leading to a shorter decay time. According to Zych et al. [24], the radiative lifetime of 5*d*–4*f* transition (in [24], Pr^{3+} was explicitly examined) is proportional to λ^3, while the proportionality factor depends also on refractive index of the material. The correlation between the determined wavelengths of the Ce^{3+} 5*d* – 4*f* emission doublet and the observed overall decay time τ is shown in Supplementary Information Fig. SI_9. Although the wavelength range is too short to ascertain if the λ^3 or λ^2 power law (see [24]) describes the data, there is a very good correlation between τ and λ^3 for all non-Gd garnets, while the Gd-containing garnets have shorter decay times than expected from this model, possibly due to some other process competing with the Ce^{3+} 5*d* – 4*f* radiative decay. Additionally, the observed decay times are slightly shorter than the values reported for single crystals or polycrystalline samples, i.e. ~ 55-60 ns for LuAG [25,26] and ~60-100 ns for YAG [25,27]. Generally, photoluminescence (i.e. radiative) decay time is often identical to a main or recognizable component within the radioluminescence decay curve, which usually is much more complex than the PL decay. Taking into account that measured photo-/radioluminescence decay times also somewhat vary based on fabrication technique, temperature or composition, the observed small decrease in decay time may be related to the preparation and/or sintering of the studied {RE}$_3$(Al,Ga)$_5$O$_{12}$:Ce samples in oxidizing atmosphere, as was reported earlier for photoluminescence decay in GGAG:Ce,Mg [28].

The luminescence of $Y_3(Al,Ga)_5O_{12}$ samples with higher Ga content (≥ 60%) was quenched at room temperature, resulting in lower PL intensity and thus, an increased noise of normalized PL spectra in Fig. 4. This quenching is caused by the thermal ionization of the Ce^{3+} 5*d* state due to the lowering of conduction band [29,30], leading to a decrease in luminescence intensity and shortening of the decay times. Moreover, the decay curves of $Y_3Al_2Ga_3O_{12}$ and $Y_3AlGa_4O_{12}$ were not adequately described by 1-exponential fit, requiring at least two exponential functions with a second, significantly faster component (~ 16% of emitted light) to be fit properly. This observation also indicates that a significant luminescence quenching occurs in those samples. No luminescence was observed from $Y_3Ga_5O_{12}$, in which even the lowest Ce^{3+} 5*d* level lies inside the conduction band [31] and electrons easily escape from the excited Ce^{3+} ion into this band.

3.3. Radioluminescence properties

The radioluminescence emission spectra of all studied samples (except "$Gd_3Al_5O_{12}$" and samples with 80 % Ga or more) excited by 17 keV X-ray beam feature an intense Ce^{3+} 5*d* – 4*f* emission band around 500 nm (see Fig. 6 and Supplementary Information Fig. SI_2 and Fig. SI_3), whose position perfectly matches the photoluminescence emission spectra (see Fig. 4 and Supplementary Information Fig. SI_1 and Tab. SI_1). The "$Gd_3Al_5O_{12}$" ($GdAlO_3$ + Al_2O_3) sample featured emission at ~ 360 nm consistent with Ce-doped perovskites instead (see Supplementary Information Fig. SI_3). Small Cr^{3+}-related peaks from the Al_2O_3 impurity and from the garnet host at ~ 695 and 688 nm as well, respectively, were observed in some *"stage 3"* sintered samples as well. In addition, a prominent Gd^{3+} 4*f* – 4*f* emission line ($^6P_{7/2} \rightarrow {}^8S_{7/2}$) at ~315 nm was present mainly in Lu-containing samples. This transition is generally completely absent in materials with high Gd content due to concentration quenching, but is rather intense in other materials; its universal presence in those samples indicates that the initial Lu_2O_3 used for synthesis might have been slightly contaminated by Gd. Decomposition of the Ce^{3+} radioluminescence emission doublet into two Gaussian components (Ce^{3+} 5*d* – $^2F_{5/2}$, 5*d* – $^2F_{7/2}$) provided transition energies with values comparable with those obtained from the photoluminescence spectra (within experimental uncertainty). Interestingly, no emission features connected with anti-site defects were observed in the radioluminescence spectra within the UV range despite the samples going through melting – this may be caused by the rather short time the studied samples spent at very high temperatures and limited thermal diffusion of rare-earth ions within the material.

The recorded radioluminescence intensity under 17 keV excitation of almost all *“stage 2”* pellets was higher or equal to the *“stage 3”* pellets. As this energy probes mainly the surface of the pellets, it should not be affected as much by the light scattering inside the pellets. The similar radioluminescence intensity of both types of pellets proves that the observed brightness is a true measure of the radioluminescence intensity of those materials. The decrease in the RL intensity of *“stage 3”* pellets was probably caused by the prolonged sintering at high temperatures, which probably oxidized some of the Ce^{3+} into generally non-luminescent Ce^{4+}. An alternative scintillation mechanism has been proposed in garnets [32], in which Ce^{4+} induced by e.g. Mg^{2+} co-doping can still produce Ce^{3+} 5*d* – 4*f* luminescence, though an excessive amount of Mg (and thus, Ce^{4+}) lowers the light yield. In $Gd_2YAl_5O_{12}$:Ce, a rather low radioluminescence intensity in the *“stage 2”* pellet that featured a visible perovskite emission as well (Supplementary Information Fig. SI_4) was observed compared to the *“stage 3”* pellet. This reflects the fact that the *“stage 2”* pellets are essentially slightly annealed as-prepared material and the $(Gd,Y)AlO_3$ perovskite phase is very stable at high temperatures. During the sintering to the *“stage 3”* pellet, the perovskite obviously decomposed into garnet, as this perovskite emission in UV was not observed in the *“stage 3”* pellets (see Fig. 6 and the Supplementary Information Fig. SI_4).

The raw recorded radioluminescence intensity under higher-energy X-ray irradiation measured at the SEALab facility is shown in Fig. 7 for both *“stage 2”* and *“stage 3”* sintered pellets. In the latter series, the brightness histograms across the sample surface were often bimodal (two Gaussian peaks) or had a long tail toward low brightness; they also featured a somewhat larger mismatch between the front and back side of most pellets. This was probably the result of a very long sintering in air at high temperatures and consequent light output inhomogeneity of the samples. The *“stage 2”* sintered pellets did not suffer from this effect and had slightly clearer trends with regard to sample composition.

In the samples with high Ga content (60 – 80 % Ga), a significant afterglow was observed as well, along with a gradual increase of the sample brightness with successive irradiations within the measurement spanning tens of minutes. All these observations result from the 5*d* levels of Ce^{3+} being much closer to the conduction band in this system [29], leading to thermal ionization of the Ce^{3+} 5*d* excited state (causing decrease in luminescence intensity) and subsequent capture of electrons on traps, including those connected with anti-site defects. The energy barrier for escape of electrons from shallow traps also decreases with Ga content, leading to delayed recombination and afterglow as well as the so-called "brightburn" or memory effect [33]. The rather long time period, over which the increase in intensity was observed, suggests the latter phenomenon as the main cause.

The main trend observed in the SEALab radioluminescence brightness of garnet pellets was a gradual decrease of brightness from $Lu_3Al_5O_{12}$ to $Y_3Al_5O_{12}$ and from $Y_3Al_5O_{12}$ to $Y_3Ga_5O_{12}$ (see Fig. 7). Although all samples were irradiated by the same X-ray beam intensity, the energy (dose) deposited within each sample varied because of their different Z_{eff} and attenuation coefficients $\mu(E)$. The latter property is proportional to sample density ρ and thus, density-independent $\mu/\rho(E)$ is tabulated for each element [34]. Therefore, this dose effect had to be taken into account and a simple model was developed, described below. Based on this model, varying absorbed dose seems to be the main reason for the decrease of brightness between $Lu_3Al_5O_{12}$ and $Y_3Al_5O_{12}$.

3.4. *Quantitative RL comparison model*

Quantitative comparison of scintillators usually revolves around light yield, the amount of photons emitted from the materials within a defined time frame divided by the energy absorbed in the material [phot. / MeV]. This value, however, cannot be measured easily and with high throughput when samples are in a powder form, as there generally is no photo-peak in pulse-height spectra due to multiple scattering processes and absorption. In order to estimate the relative light yield of materials within a self-consistent sample set, we propose to use both the radioluminescence intensity measured in the SEALab apparatus and the model described below. The desired output of the evaluation is a relative amount of detected photons per absorbed energy of continuous irradiation, i.e. the $N_{h\nu,\mathrm{det.}} / \Delta E$ value [phot. / MeV], which may be a reasonably appropriate estimator for fast screening of light yield. The derivation of the model is described below.

The photon beam with energy E is attenuated when passing through a sample and deposits part of its energy within each volume element – these values are represented by mass attenuation coefficient μ/ρ and mass energy absorption coefficient μ_{en}/ρ, respectively [34,35]. In mixtures, these values can be calculated reasonably accurately from the values of constituent elements i with weight fraction w_{i}, using the mixture rule. In the case of polychromatic beam, X-ray photons with low energy are generally attenuated more (high μ/ρ) than high-energy X-ray photons, leading to their earlier disappearance from the spectrum ("beam hardening"). The energy delivered to each volume element of the sample, represented as absorbed dose $D = \mathrm{d}E/\mathrm{d}m$, is converted into visible photons during the scintillation process. Emitted light has to escape from that volume element through the rest of the opaque sample in order to be detected. Both light generation (absorbed dose) and its extraction efficiency (visible light attenuation) depend on the depth of interaction within the sample. To correct for this effect, we assumed that visible photons are attenuated in the samples by Lambert-Beer law:

$$N_{h\nu} = N_{h\nu}^{0} \cdot \exp(-\alpha \cdot d), \qquad (1)$$

where $N_{\mathrm{h\nu}}$ is the amount of visible photons remaining from the initial value $N_{\mathrm{h\nu}}{}^{0}$ after distance d travelled within the material with optical attenuation / extinction coefficient α. Because the samples have a rather small solid angle when viewed by the camera at the SEALab facility, d was assumed to be equal to the depth of the given point within the pellet from the point of impact of X-ray beams (perpendicular distance to the sampled surface).

The energy absorbed within each thickness element dx can be calculated from the absorbed dose under assumption that for low-energy photons, absorbed dose can be approximated by the so-called collision KERMA [35]:

$$\frac{\mathrm{d}E}{\mathrm{d}x} = \frac{\mathrm{d}E}{\mathrm{d}m} \cdot \rho \cdot A = \mu_{\mathrm{en}} \cdot I \cdot E = \mu_{\mathrm{en}} \cdot I_0 \cdot E \cdot \exp\left(-\left(\frac{\mu}{\rho}\right) \cdot \rho \cdot x\right), \qquad (2)$$

where ρ is the density of a given sample, μ_{en} is mass energy absorption coefficient of the material μ_{en}/ρ multiplied by its density, I and I_0 represent the current and initial X-ray beam fluence (photons per energy interval), x stands for distance within the sample for the volume element dV = A·dx and E is the X-ray photon energy.

Then, the amount of light generated in the sample by X-ray photons with energy E and extracted during front-face imaging ($d = x$) of opaque samples was derived from (1) and (2) as:

$$N_{h\nu,\mathrm{detected}} = \int_0^L \mathrm{LY}\cdot k\cdot \frac{\mathrm{d}E}{\mathrm{d}x}\cdot \exp(-\alpha\cdot x)\,\mathrm{d}x =$$

$$= \mathrm{LY}\cdot k\cdot I_0\cdot E\cdot \int_0^L \mu_{\mathrm{en}}\cdot \exp(-\mu\cdot x)\cdot \exp(-\alpha\cdot x)\,\mathrm{d}x =$$

$$= \mathrm{LY}\cdot k\cdot I_0\cdot E\cdot \frac{\mu_{en}}{\mu+\alpha}\cdot \left(1-\exp\left(-(\mu+\alpha)\cdot L\right)\right), \quad (3)$$

where LY is the light yield of the scintillating material for a given energy E, k is a proportionality constant encompassing light detection efficiency of the detecting setup, μ is mass attenuation coefficient of the material μ/ρ multiplied by its density, and L stands for the total sample length (thickness). In polychromatic beams, equation (3) has to be integrated over the whole spectrum, E being replaced by its percentual contribution within the initial spectrum, i.e. $\%E = E\cdot N(E) / \Sigma\, N(E)$, keeping in mind that both μ and μ_{en} depend on E as well [34]. Identically derived equation for the back-face imaging configuration of the SEALab setup ($d = L - x$) is shown in Supplementary Information equation (SI_1). In a continuous X-ray irradiation, the “LY” in (3) includes also the contribution from very long decay components and afterglow; nevertheless, the LY can be estimated from it:

$$N_{h\nu,\mathrm{det.}}/\Delta E = \frac{N_{h\nu,\mathrm{detected}}}{E\cdot\frac{\mu_{\mathrm{en}}}{\mu+\alpha}\cdot\left(1-\exp[-(\mu+\alpha)\cdot L]\right)} \propto \mathrm{LY} \qquad (4)$$

Equation (3) integrated over the whole X-ray spectrum at SEALab was used to estimate the $N_{\mathrm{h\nu,det.}}$ / ΔE of the *“stage 2”* sintered samples, using light attenuation coefficient $\alpha \sim 130$ cm^{-1} (very roughly estimated from UV-Vis measurements of thinner *“stage 2”* pellets). For the *“stage 3”* pellets, their directly measured light attenuation coefficients were utilized. The values of μ/ρ and μ_{en}/ρ used for this calculation were interpolated from the NIST mass attenuation coefficients database for each energy within the GEANT4-simulated spectrum of the X-ray source used. In addition, the relative contribution of each X-ray energy within the spectrum toward the collected light can yield the mean X-ray energy contributing to the brightness; this energy ranged between ~ 45 keV ($Y_3Al_5O_{12}$) to ~ 55 keV ($Lu_3Al_5O_{12}$).

The $N_{h\nu,det.}$ / ΔE of both variants of sintered pellets are shown in Fig. 8, showing almost constant values between $Y_3Al_5O_{12}$ and $Lu_3Al_5O_{12}$ and sharp decrease with increasing Ga content in $Y_3(Al,Ga)_5O_{12}$. In both "*stage 2*" and "*stage 3*" sintered pellets, almost identical behavior was observed in this composition area, but the values for the latter seem to be slightly more scattered. Toward the Gd-rich compositions, a small decrease of $N_{h\nu,det.}$ / ΔE is observed with no clear trends; the $GdY_2Al_5O_{12}$ pellets were an exception and were exceptionally bright among all samples. To validate the seemingly erratic behavior in the $Y_3Al_5O_{12}$-$Gd_3Al_5O_{12}$-$Lu_3Al_5O_{12}$ part of the plot, a second batch of those 4 samples was prepared by melt-quenching, processed into *"stage 2"* pellets and measured at the SEALab facility. The new samples showed the same behavior as the original batch (see Supplementary Information Fig. SI_8), with $GdY_2Al_5O_{12}$ being the brightest by far, while the $Gd_2LuAl_5O_{12}$ was brighter than both remaining samples. Therefore, the observed values most probably reflect the physics of the samples or their synthesis history and are not just a random experimental variation. Based on Fig. 8, $GdY_2Al_5O_{12}$, $Y_3Al_5O_{12}$ and $LuY_2Al_5O_{12}$ seem to have the highest $N_{h\nu,det.}$ / ΔE, and thus, relative light yield, among the samples synthesized in this work.

Comparison of these observations to literature values of light yield can be somewhat misleading, as LY is usually measured in single crystal form from pulse-height spectra after excitation by a pulsed source as a number of photons collected within some specific gate (or acquisition) time. Any very slow scintillation decay component thus significantly lowers the light yield. The approach utilized in this work, however, uses continuous X-ray source and therefore includes these slow decay components as well. Nevertheless, assuming the amount of "slow light" or afterglow is similar, the comparison between different materials can still be made. The amount of afterglow can be also estimated from a separate measurement of scintillation decay curve. That being said, the ratio between estimated $N_{h\nu,det.}$ / ΔE of $Lu_3Al_5O_{12}$ and $Y_3Al_5O_{12}$ in this work is 0.85 and 0.90 for *"stage 2"* and *"stage 3"* pellets, respectively. Single crystals of $Lu_3Al_5O_{12}$:Ce are often reported to have lower light yield than $Y_3Al_5O_{12}$:Ce crystals, mainly because of larger contribution of slow decay components [25,36]. The decrease of intensity toward $Y_3Ga_5O_{12}$ clearly correlates with the effects of temperature quenching of the Ce^{3+} $5d_1$ state described above. These trends seem to agree with literature, but in order to unambiguously confirm that the observed brightness at SEALab facility corrected for absorbed dose can give a relative estimate of light yield of these materials, further experiments are needed. It might be possible to measure light yield of those rather opaque samples using pulse-height spectra even without a clear photopeak; however, this exceeds the scope of this work and will be pursued in a following study. Similarly, the behavior of the Gd-containing samples that could not be adequately explained based on the known data requires further research into.

In conclusion, quenching from the melt was shown to rapidly produce reasonably pure garnet materials, whose properties match the known behavior of these scintillator materials; their relative brightness observed by radiographic imaging apparatus seems to be suitable for estimation of their light yields relative to each other.

4. Conclusions

A series of Ce-doped $\{RE\}_3Al_5O_{12}$ and $Y_3(Al,Ga)_5O_{12}$ garnets was successfully synthesized by quenching of the melt in an Optical Floating Zone furnace, serving as a validation test of this method for high-throughput screening of scintillating oxides. The composition of all samples was determined via X-ray Powder Diffraction analysis and the garnet phase was present in all but one sample; $Gd_3Al_5O_{12}$ could not be prepared by this method due to its instability at its melting temperature and $GdAlO_3$ formed instead. In all garnet samples, the lattice parameter a changed linearly with composition and closely followed the reference values, the large Ce^{3+} ion causing a consistent slight increase over those values. At high Ga concentrations, the lattice parameters noticeably decreased, most probably because of Ga volatility at high temperatures. In order to quantitatively compare luminescence properties of these samples in the form of opaque pellets, two approaches were tested – sintering at moderate and at very high temperatures. In the former approach, dilatometer measurements were employed to obtain the sintering temperature needed for the tested materials, which proved to result in a similar densification. In the latter approach, the high temperatures involved caused spatial non-homogeneity of the emission across the pellet faces and significant difference between both sides.

All garnet samples except those with high Ga content featured an intense photoluminescence with wide Ce^{3+} 5*d* – 4*f* emission doublet peaking at ~ 500–580 nm depending on the sample composition. In radioluminescence emission spectra, an identical intense emission was observed. Its position shifted in accordance with the literature, Ga causing blue shift of the emission and substitution Lu → Y → Gd causing progressive red shift of the emission. For Ga concentrations ≥ 60 %, i.e. $Y_3Al_2Ga_3O_{12}$, the luminescence became severely quenched due to the thermal ionization of the Ce^{3+} 5*d* excited state. The energies of the two Gaussian components of Ce^{3+} 5*d* – 4*f* emission band were obtained from fits of the measured room-temperature spectra and showed reasonably linear dependence on composition, with small deviations at very high Gd content. Photoluminescence decay was found to be single exponential (apart from $Y_3Al_2Ga_3O_{12}$ and $Y_3AlGa_4O_{12}$) and the decay times mirrored the trends in the Ce^{3+} 5*d* – 4*f* transition energies, changing reasonably linearly with composition. In the samples with high Ga content, the decay became much faster and non-exponential, evidencing significant thermal quenching of the Ce^{3+} excited state.

The room-temperature radioluminescence properties of fabricated pellets were also evaluated by radiographic imaging at the SEALab facility using polychromatic X-ray beam (W anode, 225 keV end-point energy). The pellets sintered at very high temperatures had uneven brightness across their face in the collected images, whereas the pellets sintered at moderate temperatures were rather consistent. Due to the different amount of energy deposited by the X-ray beam into various samples and into different depth, a simple model for absorbed dose delivered to the samples and the light losses by attenuation was developed. Using this model, it was shown that the observed decrease of sample brightness between $Lu_3Al_5O_{12}$ and $Y_3Al_5O_{12}$ is caused mainly by the variations in absorbed dose within the samples. Among the samples tested, $LuY_2Al_5O_{12}$:Ce, $GdY_2Al_5O_{12}$:Ce and $Y_3Al_5O_{12}$:Ce showed the highest relative light yield at the given energy range (mean *E* responsible for the collected light was 45–55 keV). A very sharp decrease in relative light yield was again observed with increasing Ga concentration, suggesting that thermal ionization (quenching) occurred in those samples.

The quenching from melt and subsequent characterization of the produced polycrystalline materials in the form of pellets was shown to be a fast and reasonably reliable method for screening scintillating materials. The properties of synthesized garnets determined by rapid characterization techniques can be then used to verify scintillator prediction models or provide input for scintillator performance models.

CRediT authorship contribution statement

Bárta, J.: Formal Analysis, Investigation, Methodology, Writing - Original Draft. *Pestovich, K. S.:* Investigation, Methodology, Writing - Review & Editing. *Valdez, J. A.:* Investigation. *Wiggins, B. W.:* Investigation, Writing - Review & Editing. *Richards, C. G.:* Investigation. *Smith, E.:* Investigation. *Clayton, J. H.:* Investigation, Writing - Review & Editing. *Smalley, D.:* Resources, Writing - Review & Editing. *McClellan, K. J.:* Conceptualization, Methodology, Project administration, Resources, Supervision.

Declaration of Competing Interest

☒ The authors declare that they have no known competing financial interests or personal relationships that could have appeared to influence the work reported in this paper.

☐The authors declare the following financial interests/personal relationships which may be considered as potential competing interests:

Acknowledgements

Research presented in this article was supported by the Laboratory Directed Research and Development program of Los Alamos National Laboratory under project number 20190043DR, “Brighter, Faster, Tougher: Adaptive Co-design of Resilient Radiation Detector Materials”. Los Alamos National Laboratory strongly supports academic freedom and a researcher’s right to publish; as an institution, however, the Laboratory does not endorse the viewpoint of a publication or guarantee its technical correctness. LA-UR-21-20790.

Portions of this work were supported by Mission Support and Test Services, LLC, under Contract No. DE-NA0003624 with the U.S. Department of Energy, National Nuclear Security Administration, NA-10 USDOE NA Office of Defense Programs (NA-10). DOE/NV/03624--0963.

References

[1] Dujardin C., Auffray E., Bourret-Courchesne E., Dorenbos P., Lecoq P., Nikl M., Vasil’ev A. N., Yoshikawa A., Zhu R.-Y., 2018. Needs, trends and advances in inorganic scintillators. IEEE Trans. Nucl. Sci. 65, 1977-1997.

[2] Pilania G., Liu X.-Y., Wang Z.H., 2019. Data-enabled structure–property mappings for lanthanide-activated inorganic scintillators. J. Mater. Sci. 54, 8361-8380.

[3] Talapatra A., Uberuaga B.P., Stanek C.R., Pilania G, 2021. A machine learning approach to prediction of formability and thermodynamic stability of single and double perovskite oxides. Chem. Mater. 33, 845-858.

[4] Armbruster T., Geiger C. A., Lager G. A., 1992. Single-crystal X-ray structure study of synthetic pyrope almandine garnets at 100 and 293 K. Am. Mineral. 77, 512-521.

[5] Li J.-G., Sakka Y., 2015. Recent progress in advanced optical materials based on gadolinium aluminate garnet ($Gd_3Al_5O_{12}$). Sci. Technol. Adv. Mater. 16, 014902.

[6] Laguta V., Zorenko Y., Gorbenko V., Iskaliyeva A., Zagorodniy Y., Sidletskiy O., Bilski P., Twardak A., Nikl M., 2016. Aluminum and gallium substitution in yttrium and lutetium aluminum–gallium garnets: Investigation by single-crystal NMR and TSL methods. J. Phys. Chem. C 120, 24400-24408.

[7] Nikl M., Mihóková E., Pejchal J., Vedda A., Zorenko Y., Nejezchleb K., 2005. The antisite Lu_{Al} defect-related trap in $Lu_3Al_5O_{12}$:Ce single crystal. Phys. Status Solidi B 242, R119-R121.

[8] Li J.K, Li J.-G., Zhang Z. J., Wu X.L., Liu S.H., Li X.D., Sun X.D., Sakka Y., 2012. Gadolinium aluminate garnet ($Gd_3Al_5O_{12}$): Crystal structure stabilization via lutetium doping and properties of the $(Gd_{1-x}Lu_x)_3Al_5O_{12}$ solid solutions (x = 0–0.5). J. Am. Ceram. Soc. 95, 931-936.

[9] Luo J.L., Wu Y.T., Zhang G.Q., Zhang H.J., Ren G.H., 2013. Composition-property relationships in $(Gd_{3-x}Lu_x)(Ga_yAl_{5-y})O_{12}$:Ce (x = 0, 1, 2, 3 and y = 0, 1, 2, 3, 4) multicomponent garnet scintillators. Opt. Mater. 36, 476-481.

[10] Yoshikawa A., Fujimoto Y., Yamaji A., Kurosawa S., Pejchal J., Sugiyama M., Wakahara S., Futami Y., Yokota Y., Kamada K., Yubuta K., Shishido T., Nikl M., 2013. Crystal growth and characterization of Ce:$Gd_3(Ga,Al)_5O_{12}$ single crystal using floating zone method in different O_2 partial pressure. Opt. Mater. 35, 1882-1886.

[11] Gervais M., Le Floch S., Gautier N., Massiot D., Coutures J.P., 1997. Crystallization of $Y_3Al_5O_{12}$ garnet from deep undercooled melt: Effect of the Al-Ga substitution. Mater. Sci. Eng. B 45, 108-113.

[12] Kuwano Y., Suda K., Ishizawa N., Yamada T., 2004. Crystal growth and properties of $(Lu,Y)_3Al_5O_{12}$. J. Cryst. Growth 260, 159-165.

[13] Callister W. D., Rethwisch D. G., 2014. Materials Science and Engineering: An Introduction (9th edition). Wiley, New York.

[14] Ashurov M.K., Voronko Y., Osiko V.V., Sobol A.A., Timoshechkin M.I., 1977. Spectroscopic study of stoichiometry deviation in crystals with garnet structure, Phys. Status Solidi 42, 101-110.

[15] Petrosyan A. G., Ovanesyan K. L., Sargsyan R. V., Shirinyan G. O., Abler D., Auffray E., Lecoq P., Dujardin C., Pedrini C., 2010. Bridgman growth and site occupation in LuAG:Ce scintillator crystals. J. Cryst. Growth 312, 3136-3142.

[16] Vegard L., 1921. Die Konstitution der Mischkristalle und die Raumfüllung der Atome (in German). Z. Phys. 5, 17-26.

[17] Shannon R. D., 1976. Revised effective ionic radii and systematic studies of interatomic distances in halides and chalcogenides. Acta Crystallogr. A 32, 751-767.

[18] Tomm Y., Reiche P., Klimm D., Fukuda T., 2000. Czochralski grown Ga_2O_3 crystals. J. Cryst. Growth 220, 510-514.

[19] Seijo L., Barandiarán Z., 2014. Large splittings of the 4*f* shell of Ce^{3+} in garnets. Phys. Chem. Chem. Phys. 16, 3830-3834.

[20] Hehir J. P., Henry M. O., Larkin J. P., Imbusch G. F., 1974. Nature of the luminescence from YAG:Cr^{3+}. J. Phys. C: Solid State Phys. 7, 2241-2248.

[21] Kamada K., Endo T., Tsutumi K., Yanagida T., Fujimoto Y., Fukabori A., Yoshikawa A., Pejchal J., Nikl M., 2011. Composition engineering in cerium-doped $(Lu,Gd)_3(Ga,Al)_5O_{12}$ single-crystal scintillators. Cryst. Growth Des. 11, 4484-4490.

[22] Bárta J., Müllerová E., Kuzár M., Procházková L., Kučerková R., Jakubec I., Čuba V., 2019. Photochemical synthesis and characterization of multi-component $(Gd,Lu)_3(Ga,Al)_5O_{12}$:Ce garnet powders. Radiat. Meas. 124, 98-102.

[23] Xia Z.G., Meijerink A., 2017. Ce^{3+}-doped garnet phosphors: composition modification, luminescence properties and applications. Chem. Soc. Rev. 46, 275-299.

[24] Zych A., de Lange M., de Mello Donegá C., Meijerink A., 2012. Analysis of the radiative lifetime of Pr^{3+} d-f emission. J. Appl. Phys. 112, 013536.

[25] Chewpraditkul W., Swiderski L., Moszynski M., Szczesniak T., Syntfeld-Kazuch A., Wanarak C., Limsuwan P., 2009. Scintillation properties of LuAG:Ce, YAG:Ce and LYSO:Ce crystals for gamma-ray detection. IEEE Trans. Nucl. Sci. 56, 3800-3805.

[26] Ogiegło J.M., Zych A., Ivanovskikh K.V., Jüstel T., Ronda C.R., Meijerink A., 2012. Luminescence and energy transfer in $Lu_3Al_5O_{12}$ scintillators co-doped with Ce^{3+} and Tb^{3+}. J. Phys. Chem. A 116, 8464-8474.

[27] Zorenko Y., Mareš J.A., Průša P., Nikl M., Gorbenko V., Savchyn V., Kučerková R., Nejezchleb K., 2010. Luminescence and scintillation characteristics of YAG:Ce single crystalline films and single crystals. Radiat. Meas. 45, 389-391.

[28] Bárta J., Čuba V., Jarý V., Beitlerová A., Pánek D., Parkman T., Nikl M., 2018. Photoinduced preparation of bandgap-engineered garnet powders. IEEE Trans. Nucl. Sci. 65, 2184-2190.

[29] Fasoli M., Vedda A., Nikl M., Jiang C., Uberuaga B.P., Andersson D. A., McClellan K. J., Stanek C. R., 2011. Band-gap engineering for removing shallow traps in rare-earth $Lu_3Al_5O_{12}$ garnet scintillators using Ga^{3+} doping. Phys. Rev. B 84, 081102(R)

[30] Venevtsev I.D., Khanin V., Rodnyi P.A., Wieczorek H., Ronda C., 2018. Temperature quenching of radio- and photoluminescence of $Y_3(Ga,Al)_5O_{12}$:Ce^{3+} and $Gd_3(Ga,Al)_5O_{12}$:Ce_{3+} garnet ceramics. IEEE Trans. Nucl. Sci. 65, 2090-2096.

[31] Ueda J., Tanabe S., Nakanishi T., 2011. Analysis of Ce^{3+} luminescence quenching in solid solutions between$Y_3Al_5O_{12}$ and $Y_3Ga_5O_{12}$ by temperature dependence of photoconductivity measurement. J. Appl. Phys. 110, 053102.

[32] Nikl M., Kamada K., Babin V., Pejchal J., Pilařová K., Mihóková E., Beitlerová A., Bartosiewicz K., Kurosawa S., Yoshikawa A., 2014. Defect engineering in Ce-doped aluminum garnet single crystal scintillators. Cryst. Growth Des. 14, 4827-4833.

[33] Moretti F., Patton G., Belsky A., Fasoli M., Vedda A., Trevisani M., Bettinelli M., Dujardin C., 2014. Radioluminescence sensitization in scintillators and phosphors: Trap engineering and modeling. J. Phys. Chem. C 118, 9670-9676.

[34] Hubbell J. H., Seltzer S. M., 1995. Tables of X-ray mass attenuation coefficients and mass energy absorption coefficients: 1 keV to 20 MeV for elements Z = 1 to 92 and 48 additional substances of dosimetric interest. NIST Interagency/Internal Report 5632, NIST Standard Reference Database 126.

[35] McParland B.J., 2010. Nuclear medicine radiation dosimetry: Advanced theoretical principles. 1st ed., Springer-Verlag, London, United Kingdom; pp. 200-206, 341-344.

[36] Nikl M., 2006. Scintillation detectors for X-rays. Meas. Sci. Technol. 17, R37-R54.

Figure captions

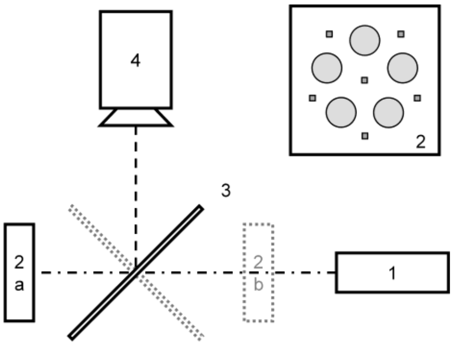

Fig. 1 – NNSS's scintillator evaluation and assessment apparatus setup: 1 – X-ray source; 2 – sample holder (2a = front-face-imaging configuration, 2b = back-face-imaging configuration); 3 – reflecting pellicle; 4 – camera.

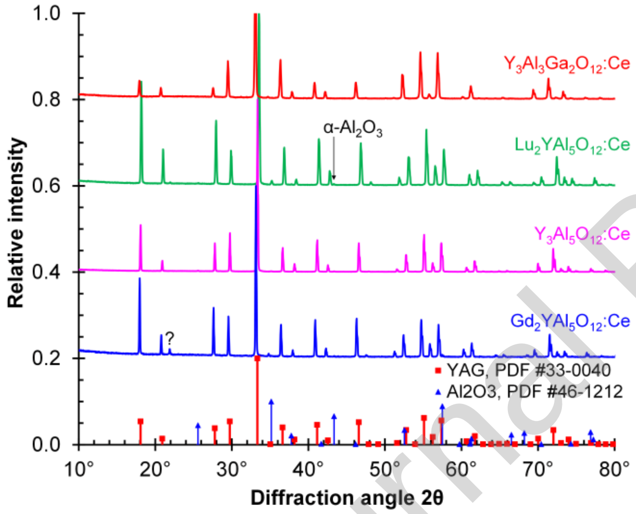

Fig. 2 – Diffraction patterns of several selected garnet samples (*"stage 3"* sintered pellets), compared to the relevant ICDD PDF-2 database files.

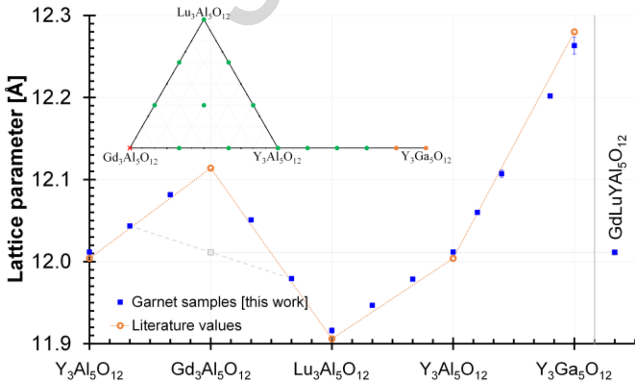

Fig. 3 – Evolution of lattice parameters *a* with the composition of the prepared garnet samples, compared to the literature values of pure end-point garnets; inset: overview of the compositional area probed.

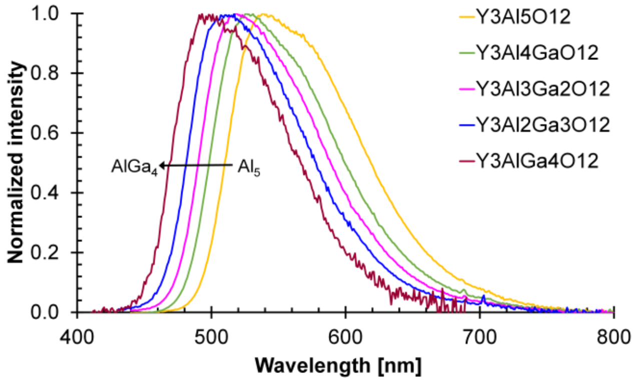

Fig. 4 – Normalized photoluminescence emission spectra of prepared garnet pellets (combined from spectra excited by 350 nm and 468 nm) showing the effect of substitution Al → Ga.

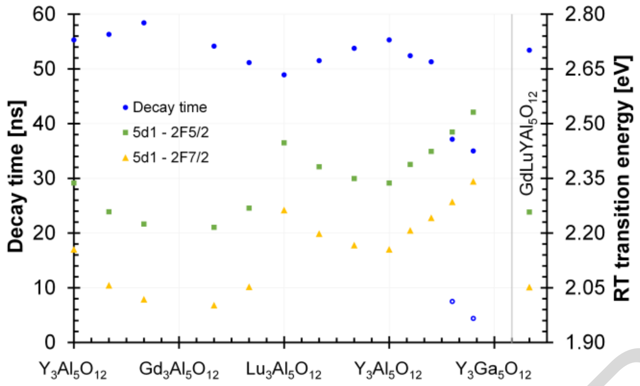

Fig. 5 – Evolution of room-temperature (RT) photoluminescence decay times and Ce^{3+} 5*d* – 4*f* transition energies of prepared garnet pellets with their composition. Empty circles show a minor fast decay component in samples with high Ga content.

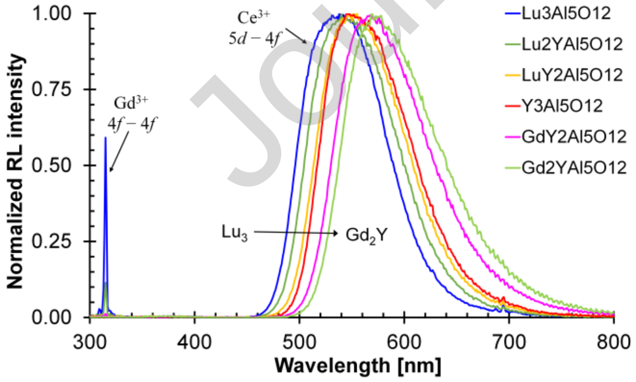

Fig. 6 – Normalized radioluminescence emission spectra of *“stage 3”* sintered pellets showing the gradual shift of emission under Lu → Y → Gd substitution in $\{RE\}_3Al_5O_{12}$:Ce.

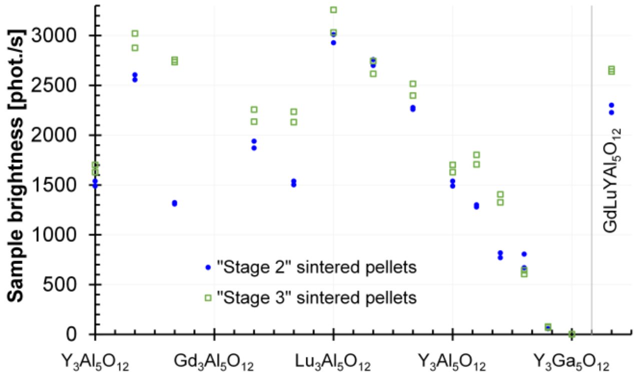

Fig. 7 – Measured sample brightness under X-ray excitation at SEALab, corrected for beam non-uniformity: solid circles – *"stage 2"* sintered pellets, empty squares – *"stage 3"* sintered pellets; both sides of each pellet were always measured.

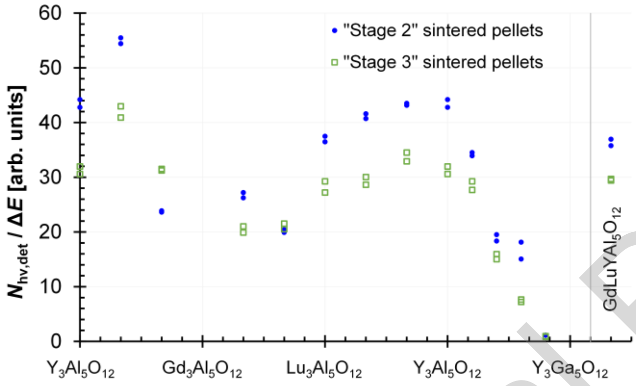

Fig. 8 – $N_{hv,det.}$ / ΔE calculated from the measured brightness of *"stage 2"* sintered pellets (solid circles) and *"stage 3"* pellets (empty squares) irradiated by X-ray photons at the SEALab facility.

Highlights

- Machine learning models for scintillator performance require self-consistent data.
- High-throughput screening needs a universal preparation technique.
- Multi-component aluminate garnets were synthesized by quenching of the melt.
- Structural and luminescence properties of powder samples were evaluated.
- A simplified model was developed for interpretation of radioluminescence intensity.